Nano Research

Open Access

Research Article

From blocker to booster: Harnessing garnet surface chemistry for advanced solid-state electrolytes

Jun Cheng[§], Xuan Zhou[§], Hongqiang Zhang, Zhen Zeng, Yuanyuan Li, Yulong Zhu, Yingsheng Liao, Lijie Ci ✉, and Deping Li ✉

State Key Laboratory of Precision Welding and Joining of Materials and Structures, School of Materials Science and Engineering, Harbin Institute of Technology (Shenzhen), Shenzhen 518055, China
[§] Jun Cheng and Xuan Zhou contributed equally to this work.

Cite this article: *Nano Research*, **2025**, *18*, 94906992. https://doi.org/10.26599/NR.2025.94906992

ABSTRACT: Garnet electrolytes with high ionic conductivity and electrochemical stability are widely used as fillers to fabricate composite solid electrolytes (CPEs) within polymer matrices. However, the performance of CPEs is significantly influenced by the surface characteristics of the garnet electrolyte. Herein, the impact of garnet surface characteristics on CPEs was systematically investigated and a conversion from a typically unstable and Lewis basic surface to a more stable Lewis acidic surface was realized, which is shown to be more conductive to the improved performance of CPEs. By simultaneously removing the Li_2CO_3 layer and applying a Li-Al-O coating, the influence of surface characteristics on CPEs was investigated. The Lewis acid Li-Al-O surface coating not only promotes lithium salt dissociation, improving the ionic conductivity and ionic transfer number, but also prevents the reformation of the passive Lewis basic Li_2CO_3 layer. Compared to garnet with a Lewis basic Li_2CO_3 surface, the garnet modified with a Lewis acid Li-Al-O coating enhances CPEs, which exhibit an improved critical current density of 1.0 mA·cm^{-2} and highly stable lithium symmetric cell cycling for 400 h at 0.2 mA·cm^{-2}. This research highlights the importance of surface chemistry in the design of high-performance solid-state batteries and presents a strategic modification approach for garnet-based CPEs.

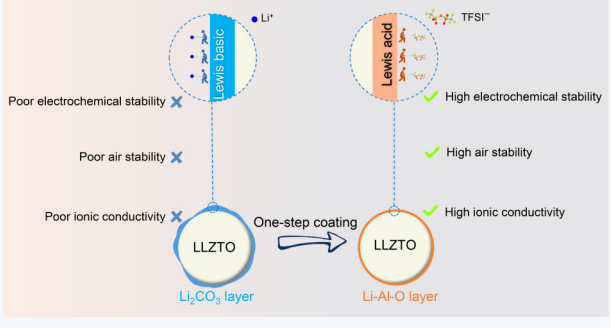

KEYWORDS: garnet electrolyte, composite solid electrolyte, surface chemistry, all-solid-state batteries

1 Introduction

The advent of solid-state batteries has marked a significant milestone in the quest for safer and higher energy density energy storage solutions [1–6]. Central to the performance of these batteries is the composite solid electrolyte (CPE), a blend of a solid polymer matrix and inorganic fillers that facilitate ionic transport [7–12]. Among various inorganic fillers, garnet electrolytes stand out due to their high ionic conductivity and electrochemical stability, making them an ideal choice for enhancing the performance of CPEs [13–16].

However, the interaction between the garnet surface and the surrounding environment is a critical, yet often overlooked, aspect that can significantly influence the overall performance of CPEs [17–22]. The garnet surface, when exposed to air, is prone to forming a Li_2CO_3 layer, which is Lewis basic and can impede lithium ion transport due to its passive nature [23–25]. This instability has been a major challenge in the widespread adoption of garnet based CPEs [20].

In this work, the impacts of garnet surface characteristics on the performance of CPEs were systematically investigated, which reveals that converting the surface of garnet from a Lewis basic to a Lewis acidic one can dramatically improve the performance of CPEs. We achieve this conversion through a novel surface modification technique that involves the simultaneous removal of the Li_2CO_3 layer and the application of a Li-Al-O coating. This one-step process not only mitigates the negative impact of the Li_2CO_3 layer but also introduces a surface that actively promotes lithium salt dissociation, thereby enhancing ionic conductivity and the lithium-ion transfer number.

The Li-Al-O modified garnet was demonstrated significantly

Received: June 19, 2024; **Revised:** July 26, 2024
Accepted: August 19, 2024

✉Address correspondence to Deping Li, lideping@hit.edu.cn; Lijie Ci, cilijie@hit.edu.cn

outperforms the traditional garnet with a Lewis basic Li_2CO_3 surface. The modified CPEs exhibit an improved critical current density (CCD) of 1.0 mA·cm^{-2} and display a highly stable lithium symmetric cell cycling for 400 h at 0.2 mA·cm^{-2}. These results highlight the critical role of surface chemistry in the design of high-performance solid-state batteries and present a strategic modification approach for garnet based CPEs.

2 Results and discussion

As illustrated in Fig. 1(a), a one-step encapsulation method is used to remove lithium carbonate and generate Li-Al-O. This process transforms the original surface, which has low ionic conductivity and low air stability, into one with high ionic conductivity and high air stability. As depicted in Fig. 1(b), the X-ray diffraction (XRD) patterns of pristine $Li_{6.4}La_3Zr_{1.4}Ta_{0.6}O_{12}$ (LLZTO) (P-LLZTO) show prominent characteristic peaks of Li_2CO_3 at 21.3°, 30.6° and 36.9° [24]. Following coating process, these peaks vanish, indicating the successful removal of Li_2CO_3 from the LLZTO surface [26]. However, no significant peaks from aluminum-based materials are detected post-coating, suggesting an amorphous nature of the coating layer. In Fig. S1 in the Electronic Supplementary Material (ESM), high-resolution transmission electron microscopy (TEM) images reveal a 3–5 nm amorphous layer on the LLZTO surface, which is coated with an aluminum base material (Li-Al-O coated LLZTO (A-LLZTO)). In contrast, the P-LLZTO surface exhibits an Li_2CO_3 layer, indicating a substantial amount of Li_2CO_3 on the P-LLZTO [27]. Raman spectra further confirm the effective removal of Li_2CO_3, as evidenced by the absence of characteristic peaks after the coating process. As shown in Fig. 1(c), Raman characteristic peaks at 680 and 1080 cm^{-1} of P-LLZTO corresponding to the bending and stretching vibrations of CO_3^{2-}, respectively, indicating the presence of a large amount of Li_2CO_3 on the surface of P-LLZTO [28]. A-LLZTO did not show obvious CO_3^{2-} vibrational scattering peak after coating, further validating the effectiveness and feasibility of the coating for removing Li_2CO_3 from the surface of LLZTO. Additionally, the high-angle annular dark-field (HAADF) images in Fig. 1(d), obtained by TEM, unveil a smooth coating layer on the surface of the P-LLZTO. As illustrated in Fig. 1(e), TEM elemental mapping images indicate uniform distribution of La, Zr, Ta and Al elements in the particle regions, suggesting a uniform coating on the original LLZTO. Further X-ray

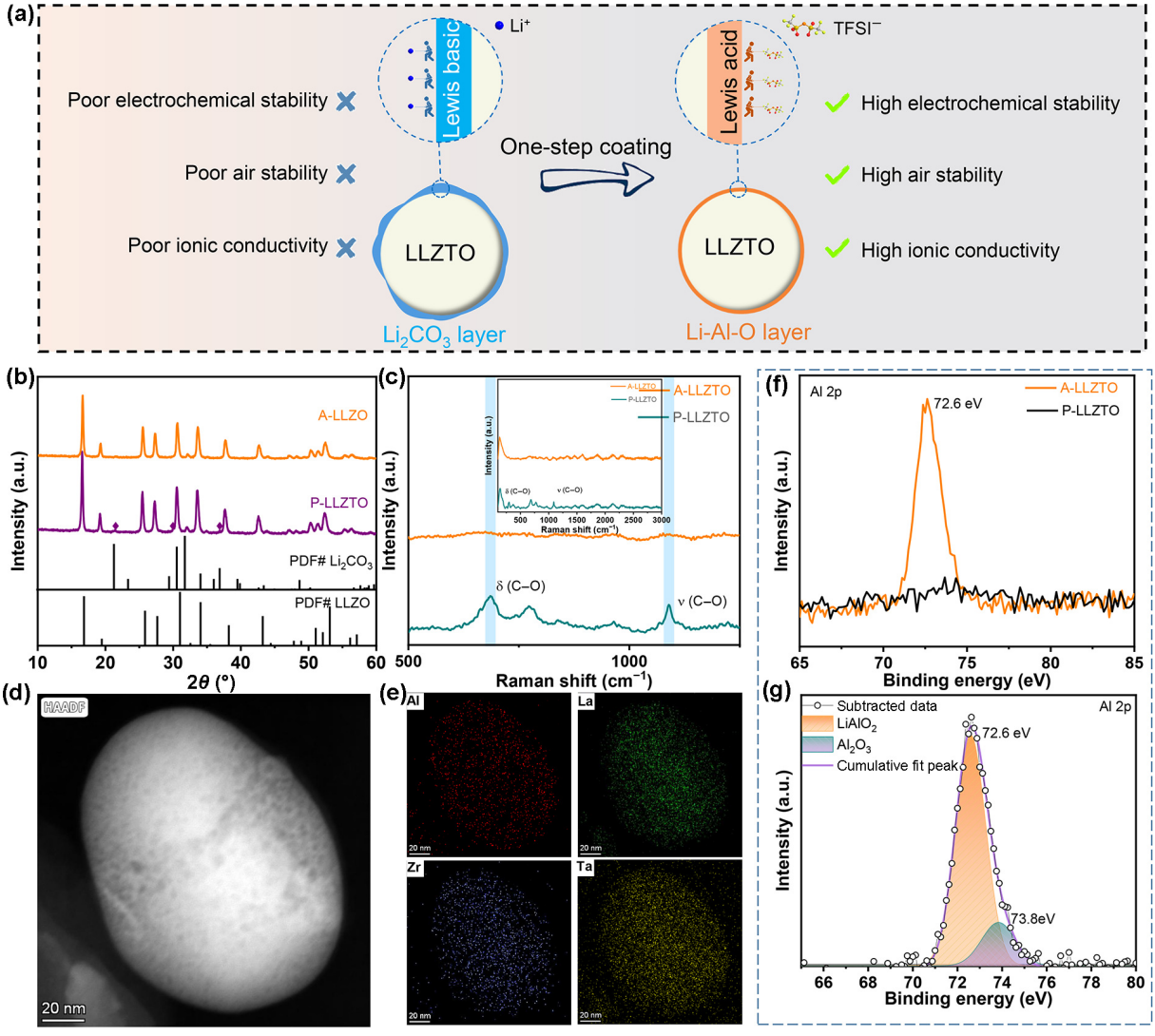

Figure 1 (a) Schematic diagram of the advantages of surface coating transformation. (b) XRD patterns and (c) enlarged Raman spectra of A-LLZTO (aluminum base material coated LLZTO) and P-LLZTO (inset image: complete Raman spectra). (d) HAADF image and (e) corresponding elemental distribution maps of LLZTO after coating. (f) Al 2p XPS spectra of A-LLZTO and P-LLZTO. (g) XPS spectrum of A-LLZTO after peak deconvolution.

photoelectron spectroscopy (XPS) spectrum analysis was conducted on A-LLZTO and original P-LLZTO to determine the composition of the obtained coating layer. As depicted in Fig. 1(f), the XPS spectra of Al 2p on the surface of the original P-LLZTO did not display obvious characteristic peaks within the binding energy range of 65–85 eV. However, as shown in Fig. 1(g), the XPS spectra of Al 2p on the surface of the coated A-LLZTO exhibited peaks at binding energies of 72.6 and 73.8 eV after fitting, corresponding to the binding energy of $LiAlO_2$ and Al_2O_3, respectively [29, 30]. This suggests the coating layer is primarily composed of $LiAlO_2$, mixed with Al_2O_3. The amorphous nature of the coating layer, as indicated by the XRD in Fig. 1(b), led to its designation as Li-Al-O in the subsequent sections.

To verify the strengths of Li-Al-O coating layer and investigate the influence of different surface properties of LLZTO on enhancing the effect of composite solid electrolyte, fresh LLZTO treated with acid (free LLZTO (F-LLZTO)) was used as a control sample for comparison with P-LLZTO and A-LLZTO. As shown in Figs. S2(a) and S2(b) in the ESM, the XRD patterns and Raman spectra indicate the successful removal of Li_2CO_3 [26]. Scanning electron microscopy (SEM) images before and after acid treatment in Figs. S2(c) and S2(d) in the ESM suggest no significant changes in particle size and morphology after acid treatment. Figures S3 and S4 in the ESM demonstrate that the optimal concentration of A-LLZTO is 30 wt.%. Consequently, this ratio has been designated as the preferred specimen for subsequent experimental analysis.

As illustrated in Figs. 2(a) and 2(b), electrochemical impedance spectroscopy (EIS) testing and the calculation of ionic conductivity revealed that the ionic conductivity of A-LLZTO@polyethylene oxide (PEO) (ALP) reached 1.4×10^{-4} S·cm^{-1}, twice as high as that of P-LLZTO@PEO (PLP) (0.6×10^{-4} S·cm^{-1}) and higher than that of F-LLZTO@PEO (FLP) (0.9×10^{-4} S·cm^{-1}). This indicates that the Li-Al-O coating not only eliminates the negative effects of the Li_2CO_3 passivation layer but is even more effective in improving the ionic conductivity of composite solid electrolytes than F-LLZTO treated with acid. As shown in the linear sweep voltammetry (LSV) test results in Fig. 2(c), ALP exhibits a high oxidative decomposition voltage of up to 4.75 V, indicating higher oxidative stability. As illustrated in Figs. 2(d)–2(f), ALP shows the highest lithium-ion transfer number of 0.14, higher than that of FLP at 0.10 and far higher than that of PLP at 0.08. The addition of ionic liquid, which brings a large number of anions and cations, results in relatively low overall ion mobility of the sample.

As illustrated in Fig. S5 in the ESM, Li_2CO_3 dissolves under conditions of pH 4.4 and 70 °C to produce CO_2 and lithium ions, which combine with aluminum ions to form Li-Al-O. To further investigate the enhancement mechanism of performance of A-LLZTO. Furthermore, the zeta potential test results in Fig. 3(a) demonstrate that the Li-Al-O coating layer is Lewis acidic. The zeta potential results show that the zeta potential of A-LLZTO, P-LLZTO and F-LLZTO is +20.7 mV, −30.3 mV and +3.8 mV, respectively, which indicates the P-LLZTO surface retains a large amount of Lewis basic Li_2CO_3 passivation layer, which may anchor lithium ions, thereby hindering their migration in composite solid electrolytes. The Li-Al-O surface shows a Lewis acidic nature, which could effectively adsorb bis(trifluoromethanesulfonyl)imide anion ($TFSI^-$) and promote the lithium salt dissociation in the composite solid electrolyte. This is further supported by the Raman spectra results of the composite electrolyte. As illustrated in Fig. 3(b), Raman spectra reveal that the S–N bond stretching band for $TFSI^-$ lies within the range of 730–760 cm^{-1} [27, 31]. After peak deconvolution, two vibrational peaks are obtained at 737 and 745 cm^{-1}, corresponding to the free $TFSI^-$ ions and the close ion pairs ($TFSI^-$ interacting with a Li^+), respectively [32]. The close ion pairs can be attributed to the undissociated lithium salt in the PLP, while the free ions correspond to the dissociated portion of anions as well as the anions in the ionic liquid [33, 34]. In the FLP, the peak corresponding to the free $TFSI^-$ ions at 737 cm^{-1} increases and the vibrational peak corresponding to the close ion pairs at 745 cm^{-1} decreases, indicating that more lithium salt is dissociated in the FLP composite solid-state electrolyte, releasing more free $TFSI^-$ ions [32]. Therefore, the presence of F-LLZTO effectively promotes the

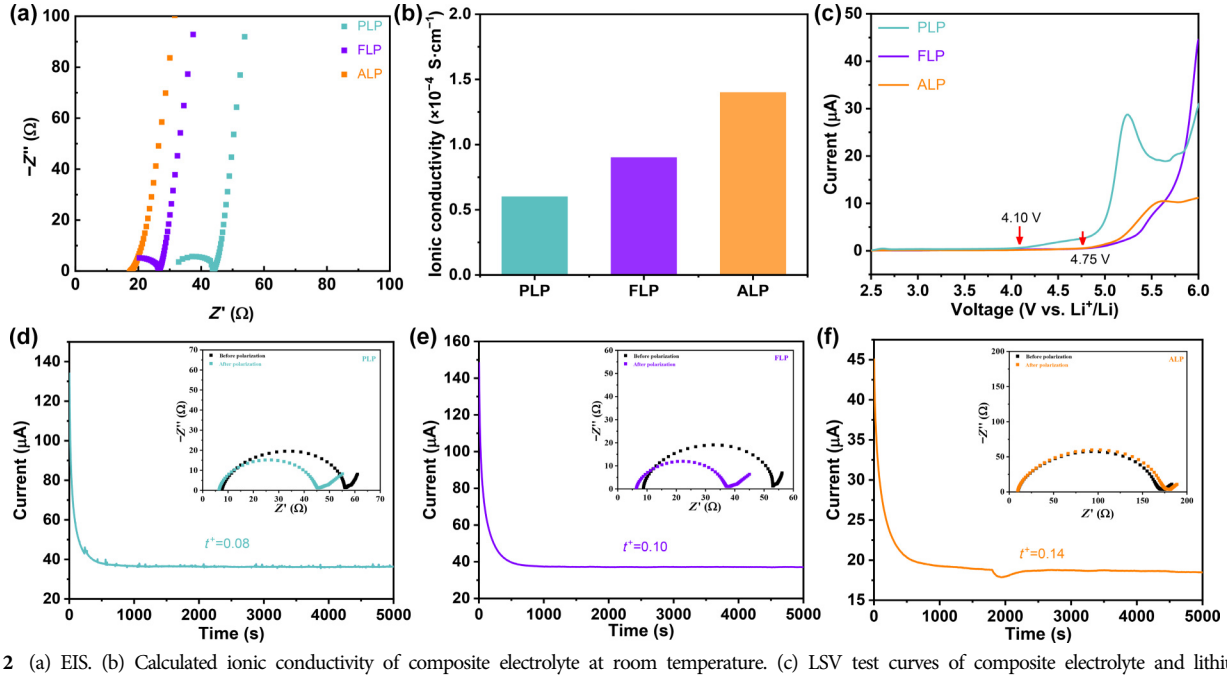

Figure 2 (a) EIS. (b) Calculated ionic conductivity of composite electrolyte at room temperature. (c) LSV test curves of composite electrolyte and lithium-ion transference number test of (d) PLP, (e) FLP and (f) ALP at 60 °C.

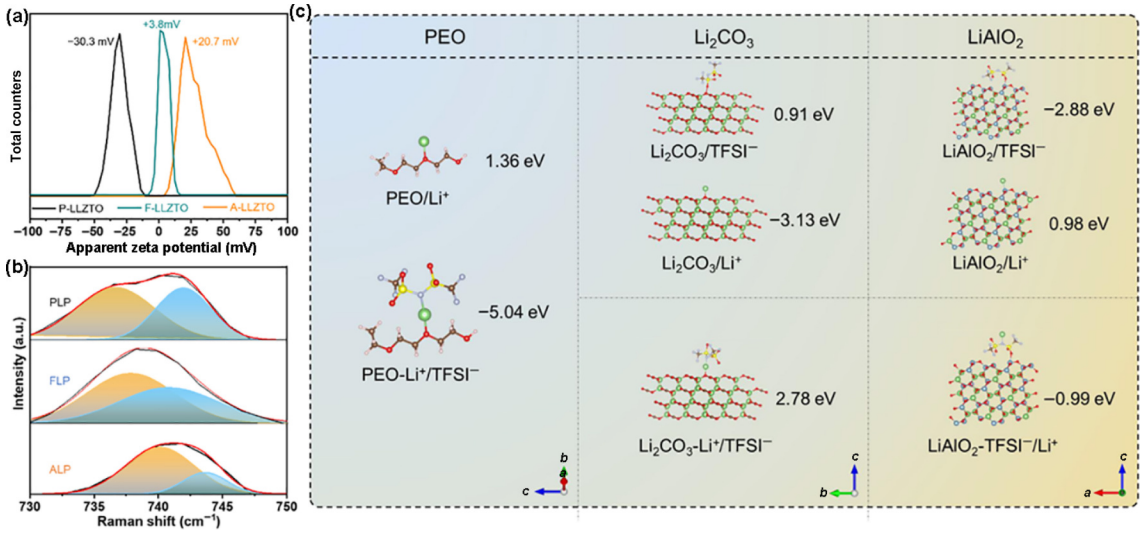

Figure 3 (a) Zeta potential test of P-LLZTO, F-LLZTO and A-LLZTO. (b) Raman spectra of PLP, FLP and ALP. (c) Calculated binding energy of the Li^+ and $TFSI^-$ adsorbed on various surface.

dissociation of lithium salts compared to P-LLZTO. In the ALP, the Raman spectra show a blue shift in the S–N bond peak, indicating the formation of more loose ion pairs (741 cm^{-1}) where $TFSI^-$ interacts indirectly with Li^+ [32]. This can be attributed to more dissociated lithium salts, where Li^+ ions form a solvation structure similar to $TFSI^-$ solvation with the ionic liquid [34]. Meanwhile, the decrease in the peak area at 745 cm^{-1}, corresponding to the close ion pairs, suggests an increased dissociation of lithium salts, releasing lithium ions which are then solvated by the ionic liquid. With an increased amount of ionic liquid participating in the lithium ion transport, this process enhances both the ionic conductivity and the lithium-ion transference number [18]. These results confirm the role of Li-Al-O-coated garnet in promoting the dissociation of lithium salts and anchoring anions.

Density functional theory (DFT) was employed to calculate the interactions between Li^+ ions and $TFSI^-$ anions with Li_2CO_3 and $LiAlO_2$ surfaces. This calculation aimed to investigate the adsorption effects of different surface properties on the cations and anions of lithium salts. As depicted in Fig. 3(c), the adsorption energy of $TFSI^-$ on the Li_2CO_3 surface is 0.91 eV, while that of Li^+ is −3.13 eV, indicating that the Li_2CO_3 surface has a greater affinity for adsorbing lithium salt cations (Li^+), which hinders the transport of lithium ions. Conversely, the adsorption energy of $TFSI^-$ on the $LiAlO_2$ surface is −2.88 eV and that of Li^+ is +0.98 eV, suggesting that the $LiAlO_2$ surface is more inclined to anchor lithium salt cations (Li^+). Further calculation results reveal that the binding energy between Li^+ adsorbed on Li_2CO_3 and free $TFSI^-$ is +2.78 eV. In contrast, the binding energy between $TFSI^-$ adsorbed on $LiAlO_2$ and free Li^+ is −0.99 eV. This is in comparison to the binding energy of Li^+ and free $TFSI^-$ adsorbed by PEO, which is significantly higher at −5.04 eV. This indicates that both the Lewis basic Li_2CO_3 and the Lewis acidic $LiAlO_2$ significantly reduce the tendency of Li^+ ions to bind with $TFSI^-$ anions, effectively promoting the dissociation of lithium salts [35, 36]. The results of DFT calculations are consistent with the measurements of lithium ion transfer numbers. Adsorption of $TFSI^-$ on $LiAlO_2$ weakens the interaction between Li^+ ions and $TFSI^-$ anions, thereby releasing more active Li^+ ions and increasing their concentration [37]. Moreover, absorbed $TFSI^-$ cannot act as a charge carrier, which further enhances the lithium ion transfer number [38].

As shown in Fig. S6 in the ESM, the modified ALP has demonstrated an increase in both the elastic modulus and tensile strength when compared to PLP, which may indicate a better ability to suppress lithium dendrites. Therefore, lithium symmetric cells were assembled to investigate the influence of various surface properties of LLZTO on the stability of CPEs towards lithium. The CCD of the PLP symmetric cell is 0.6 mA·cm^{-2} (Fig. 4(a)). Conversely, the FLP symmetric cell exhibits a higher CCD than PLP, reaching 0.8 mA·cm^{-2} (Fig. 4(b)). Lithium symmetric cells assembled with A-LLZTO, due to their high ion conductivity and lithium-ion transference number, demonstrate a higher CCD of 1 mA·cm^{-2} (Fig. 4(c)), compared to the original F-LLZTO. After cycling, the batteries were disassembled to characterize the surface morphology of the lithium metal anode. The surface of the lithium anode in Li/PLP/Li shows roughness and numerous protrusions (Fig. 4(d)), suggesting uneven lithium metal deposition, potentially leading to short-circuiting [39]. The surface of the lithium anode corresponding to Li/FLP/Li appears relatively smooth (Fig. 4(e)), but still exhibits some protrusions. The above results suggest that the presence of Lewis basic Li_2CO_3 significantly impedes the benefits of LLZTO as a filler for enhancing CPE performance. Eliminating Li_2CO_3 from the surface of LLZTO unlocks its potential to enhance CPE performance. Furthermore, the lithium foil surface corresponding to Li/ALP/Li after cycling exhibits a smooth lithium deposition surface (Fig. 4(f)). Additionally, symmetric cells assembled with ALP show stable cycling for over 400 h at a current density of 0.2 mA·cm^{-2}, whereas those assembled with PLP only cycle for 275 h before experiencing a short circuit (Fig. S7 in the ESM). The extended cycle life of symmetric cells, attributed to the high lithium-ion conductivity and transference number, ensures uniform lithium-ion flow, thus ensuring uniform lithium deposition.

The effects of different surface characterizations on the performance of composite polymer electrolytes (CPEs) in $LiFePO_4$ (LFP)/Li all-solid-state batteries were investigated through further assembly with PLP and ALP, as shown in Fig. 5(a). When ALP was utilized, it was observed that superior rate performance (as shown in Figs. 5(b) and 5(c)) and a longer cycling life (as demonstrated in Fig. 5(d)) were achieved, indicating beneficial impact of ALP on ion conductivity and lithium-ion transference number in the full cell.

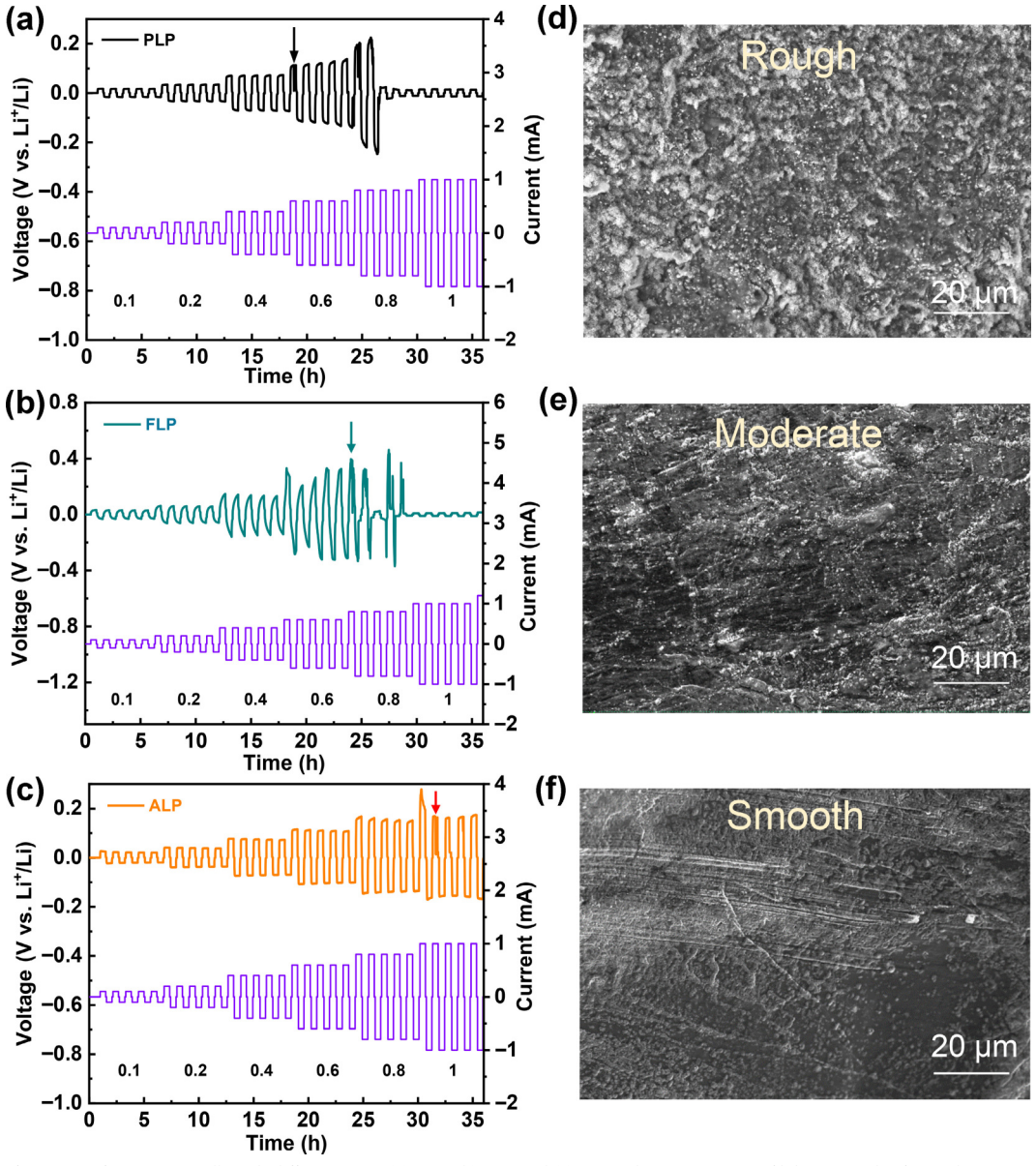

Figure 4 The performance of symmetric cells with different CPEs (a) PLP, (b) FLP and (c) ALP. The SEM images of lithium anode after cycling in symmetric cells with different CPEs (d) PLP, (e) FLP and (f) ALP

Furthermore, the faster capacity decay and greater polarization observed in the LFP/PLP/Li configuration (as shown in Figs. 5(e) and 5(f)) suggest that ALP, compared to PLP, exhibits better stability with electrodes. These results demonstrate that our Li-Al-O coating method on LLZTO effectively removes surface Li_2CO_3 passivation layers and provides a Lewis acidic surface, which enhances the ion conductivity and lithium-ion transference number of composite electrolytes. This ensures a high CCD for composite solid-state electrolytes, as well as excellent rate performance and cycling stability for the assembled full cells. It also confirms the significant impact of the Lewis acidic and basic surface properties of active fillers on enhancing the performance of composite solid-state electrolytes. Therefore, precise control of the surface properties of active fillers is crucial for enhancing the performance of composite solid-state electrolytes. The air stability of the coated LLZTO was tested (as shown in Fig. S8 in the ESM) by exposing both acid-treated and Li-Al-O coated LLZTO to air at 70% humidity for two weeks. XRD patterns revealed clear characteristic peaks of Li_2CO_3 in the uncoated LLZTO, whereas the Li-Al-O coated LLZTO showed no significant Li_2CO_3 peaks. This indicates that this coating method can significantly improve the air stability of LLZTO.

3 Conclusion

In summary, it was demonstrated that the surface passivation layer of Li_2CO_3 significantly hinders the potential of LLZTO as an active filler to enhance the performance of composite polymer electrolytes (CPEs). A one-step method has been developed that transforms this passivation layer into a lithium-ion conductor, Li-Al-O. This approach effectively removes Li_2CO_3 from the surface of LLZTO while forming an amorphous Li-Al-O coating layer. Furthermore, air stability tests have confirmed that the Li-Al-O coating significantly enhances the air stability of LLZTO compared to that of the acid-treated fresh LLZTO. Zeta potential measurements determined the different Lewis acid-base properties of various

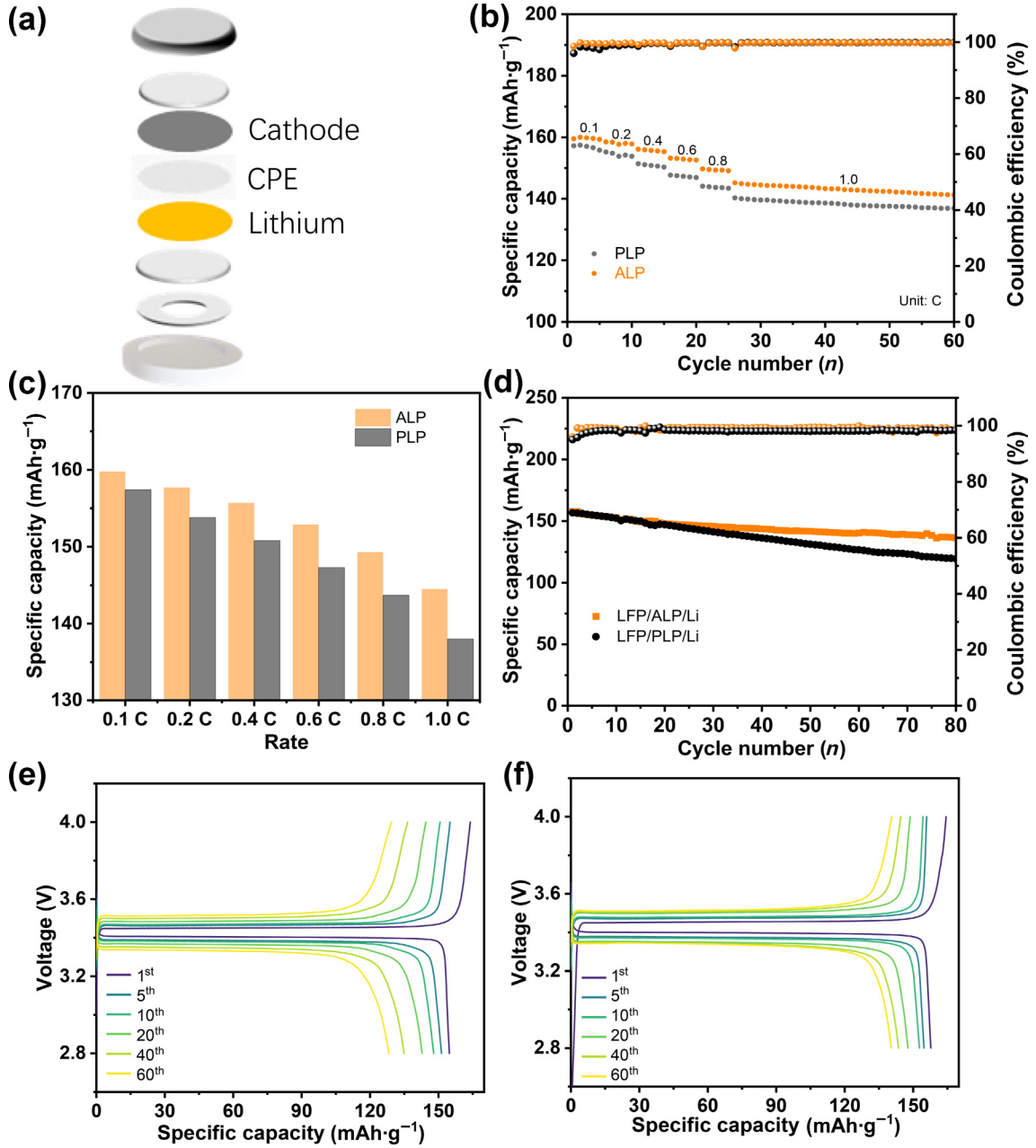

Figure 5 (a) Schematic diagram of the structure of the LFP/Li cell. (b) Rate performance and (c) corresponding specific capacity value at various rates. (d) Cycling performance at 0.2 C of LFP/CPEs/Li and corresponding charge/discharge profiles of (e) LFP/PLP/Li and (f) LFP/ALP/Li full cells.

LLZTO surfaces and based on these findings, we systematically studied the impact of LLZTO surface characteristics on the performance of composite solid-state electrolytes. A-LLZTO with Lewis acidity exhibited the highest ionic conductivity, the greatest oxidative stability and a higher lithium-ion transference number. Additionally, symmetric cells and full batteries assembled with A-LLZTO demonstrated higher critical current densities, extended cycling life, superior rate performance and improved cycling stability. In conclusion, the one-step method for coating LLZTO with Li-Al-O effectively enhances CPE performance by eliminating the surface Li_2CO_3 and systematically studying its impact on the characteristics of composite solid-state electrolytes. This highlights the importance of precise control over the surface properties of active fillers in enhancing the performance of composite solid-state electrolytes.

4 Experimental

4.1 Synthesis of nano-LLZTO powder

Stoichiometric amounts of lithium carbonate (Li_2CO_3, Aladdin, 99.99%, with a 10% surplus), lanthanum oxide (La_2O_3, Aladdin, 99.99%), zirconium dioxide (ZrO_2, Aladdin, 99.99%, particle size ranging from 0.2 to 0.4 μm) and tantalum pentoxide (Ta_2O_5, Aladdin, 99.99%) were thoroughly mixed in a zirconium dioxide (ZrO_2) ball milling jar. The jar was filled with an appropriate volume of yttria-stabilized zirconia (YSZ) balls and isopropanol to facilitate the milling process. A planetary ball mill (MITR YXQM-2L) was employed for the homogenization of the material and refinement of particle size, operating at a rotation speed of 200 rpm for a duration of 5 h. Following the milling process, the isopropanol

was evaporated from the resultant powder under controlled conditions in an oven. The powder was then positioned in an alumina crucible and subjected to sintering at a temperature of 950 °C for 2 h within a muffle furnace. Subsequently, the obtained powder underwent further refinement through additional ball milling at a speed of 200 rpm for 12 h. A slurry was formed by incorporating isopropanol into the micron-sized LLZTO powder, achieving a solid content of 20%. A sand mill (Boyee NMM-1L) was utilized for the subsequent particle size refinement, operating at 2200 rpm for 15 min. After milling, the resulting slurry was dried to yield the P-LLZTO powder. The particle size of the obtained P-LLZTO was measured to be 300 nm (D50: median particle diameter), as depicted in Fig. S9 in the ESM.

4.2 Preparation of Li_2CO_3-F-LLZTO, A-LLZTO and P-LLZTO

Initially, a 0.3 mol·L^{-1} solution of ammonium formate was prepared by dissolving it in deionized water. The pH of the solution was meticulously adjusted to 4.4 by the gradual addition of acetic acid. Subsequently, LLZTO was dispersed in ethanol and subjected to ultrasonication for 30 min to ensure a uniform dispersion. This LLZTO suspension was then introduced into the ammonium formate solution and the mixture was heated to 70 °C utilizing an oil bath. Following this, aluminum sulfate ($Al_2(SO_4)_3$) was added to the combined solution at a mass ratio of 1:5 relative to LLZTO. After 15 min of magnetic stirring, the mixture was centrifuged at 5000 rpm for 5 min to separate the components. As shown in Fig. S10 in the ESM, with 30 min coating process results in the transformation of the cubic garnet phase into the pyrochlore $La_2Zr_2O_7$ phase. The resulting powder was then sequentially washed with deionized water and ethanol, with additional centrifugation steps to remove any residual ions. Finally, the centrifuged material was heat-treated at 80 °C in a vacuum drying oven for 3 h to eliminate any remaining water and ethanol, yielding the A-LLZTO. Notably, the F-LLZTO was obtained by omitting the addition of $Al_2(SO_4)_3$ in the aforementioned process. As for P-LLZTO, to ensure the consistency of the thickness of the Li_2CO_3 passivation layer generated on the surface of LLZTO, the F-LLZTO was placed in a closed environment with an indoor humidity of 70% for two weeks and then transferred to a glove box for storage.

4.3 Preparation of composite polymer electrolytes (CPEs)

CPEs were prepared employing a conventional casting technique. Specifically, 1 g poly(ethylene oxide) (PEO, M_W = 600,000, Sigma) and lithium bis(trifluoromethanesulfonyl)imide (LiTFSI, with an ethylene oxide (EO):Li molar ratio of 30:1) were dissolved in acetonitrile to form a homogeneous solution. To this solution, 200 μL of 1-butyl-3-methylimidazolium TFSI (BMIMTFSI, Sigma-Aldrich) ionic liquid and LLZTO filler (either P-LLZTO, F-LLZTO, or A-LLZTO) were added and stirred for 12 h to ensure thorough mixing. The resulting solution was then cast into a polytetrafluoroethylene (PTFE) mold and allowed to dry at room temperature, followed by solvent evaporation at 60 °C in an inert atmosphere. The CPEs were then cut to the required sizes for subsequent use. As shown in Fig. S11 in the ESM, the CPE has a thickness of 75 μm.

4.4 Characterization of LLZTO powder and CPEs

The XRD patterns of the prepared powders were obtained using an X-ray diffractometer (PANalytical/Aeris) with Cu Kα radiation over a 2θ range of 10° to 80°. A Raman spectrometer (Renishaw InVia) and a TEM (JEM-3200FS) were utilized to examine the powders and ceramics, respectively, with the aim of confirming the removal of Li_2CO_3 and the presence of the Li-Al-O coating layer. The microstructure of the as-prepared powders and CPEs was observed using SEM (ZEISS SUPRA55). The zeta potential of the powders was assessed using a nanoparticle size and zeta potential analyzer (ZETASIZER Nano-ZS90).

EIS measurements on the different types of CPEs were conducted using a CHI660 electrochemical workstation over a frequency range from 0.1 Hz to 1 MHz. Sandwich-like stainless steel (SS)/CPEs/SS block cells were assembled for EIS testing. The ionic conductivity (σ) of the CPEs was determined using Eq. (1)

$$\sigma = \frac{l}{RS} \tag{1}$$

where l is the thickness of the CPEs in cm, R is the bulk resistance in Ω and S is the effective contact area of the electrolyte with the block electrodes in cm^2. LSV testing of Li/CPEs/SS cells was performed using a CHI660E electrochemical workstation at room temperature with a scan rate of 0.1 mV·s^{-1}, ranging from the open-circuit voltage to 6 V. The lithium-ion transference number of the materials was measured at 25 °C using the same workstation. A constant voltage of 10 mV was applied until a stable current value was reached in the lithium symmetric cell. The lithium transference number (t_{Li^+}) was calculated using the following Eq. (2)

$$t_{Li^+} = \frac{I_{SS}(\Delta V - I_0 R_0)}{I_0(\Delta V - I_{SS} R_{SS})} \tag{2}$$

where ΔV is the applied constant voltage (10 mV), I_0 is the initial current, I_{SS} is the steady-state current and R_{SS} and R_0 are the interfacial resistances after and before polarization, respectively.

4.5 Assembly and electrochemical testing of Li symmetric cells and LFP/Li full cells

Li symmetric cells and LFP/Li full cells were assembled in 2032-type coin cells. The symmetric cells consisted of lithium metal sandwiched between CPEs, while the full cells featured an LFP cathode in place of the lithium foil on the positive electrode side. The LFP cathode was prepared using a standard slurry casting method, where LFP, Super-P and polyvinylidene fluoride (PVDF) were dissolved in N-methyl-2-pyrrolidone (NMP) solvent in a weight ratio of 8:1:1 to form a uniform cathode slurry. After stirring for 10 h, the slurry was coated onto aluminum foil using a doctor blade and then vacuum dried at 110 °C for 12 h. The LFP cathode had a mass loading of 3 mg·cm^{-2}. All cells were assembled in an argon-filled glovebox with H_2O and O_2 levels below 0.01 ppm. The full cells and Li symmetric cells were tested using a LAND 2001A battery testing system at 60 °C.

4.6 DFT calculation

First-principles calculations in the framework DFT are performed by using the Vienna *ab initio* simulation package (VASP) with the projector augmented wave (PAW) method [40]. The exchange-correlation energy was calculated by using the generalized gradient approximation (GGA) of Perdew–Burke–Ernzerhof (PBE) [41]. To correct the van der Waals interactions, the DFT-D3 method proposed by Grimme et al. was adopted [42]. The energy cutoff is set to 400 eV. Spin polarization effects are considered in this study. We performed structural optimization until the residual forces on

each ion converged to less than 0.01 eV·Å^{-1}. The adsorption energy for surface hydrogen adsorbates is defined as follows:

$$\Delta E = E_{adsorption} - E_{surface} - E_{molecule} \quad (3)$$

where $E_{adsorption}$ represents the energy of the surface with the adsorbed hydrogen atom, $E_{surface}$ represents the energy of the pure surface and $E_{molecule}$ represents the energy of the Li and TFSI species in the gas phase. The calculation also includes entropy (S) and zero-point energy (E_{ZPE}) to obtain the Gibbs free adsorption energy of hydrogen

$$\Delta G_H = \Delta E_H + \Delta E_{ZPE} - T\Delta S \quad (4)$$

Electronic Supplementary Material: Supplementary material (TEM images, physicochemical properties, air stability and particle size testing of F-LLZTO, the ionic conductivity and lithium ion transference number testing of ALPs with varying ratios, the thickness and mechanical property testing of ALPs, the symmetric cell testing and the investigation of the effect of coating time on the crystal structure of LLZTO) is available in the online version of this article at https://doi.org/10.26599/NR.2025.94906992.

Data availability

All data needed to support the conclusions in the paper arepresented in the manuscript and the Electronic SupplementaryMaterial. Additional data related to this paper may be requestedfrom the corresponding author upon request.

Acknowledgements

This work was supported by National Natural Science Foundation of China (No. 52002094), Shenzhen Science and Technology Program (Nos. JCYJ20210324121411031, JSGG20210802 1253804014 and RCBS20210706092218040), the Shenzhen Steady Support Plan (Nos. GXWD20221030205923001 and GXWD20201230155427003-20200824103000001) and State Key Laboratory of Precision Welding & Joining of Materials and Structures (Nos. 24-Z-17 and 24-T-08).

Declaration of competing interest

All the contributing authors report no conflict of interests in this work.

Author contribution statement

J. C.: Conceptualization, data curation, formal analysis, investigation, methodology, visualization, writing – original draft. X. Z.: Data curation, formal analysis, investigation, methodology, visualization. H. Q. Z.: Data curation, formal analysis, methodology, visualization. Z. Z.: Formal analysis, investigation, visualization. Y. Y. L.: Formal analysis, investigation, visualization. Y. L. Z.: Formal analysis, investigation, visualization. Y. S. L.: Formal analysis, investigation, visualization. L. J. C.: Conceptualization, funding acquisition, supervision, writing – review & editing. D. P. L.: Funding acquisition, supervision, writing – review & editing. All the authors have approved the final manuscript.

Use of AI statement

None.

References

[1] Janek, J.; Zeier, W. G. Challenges in speeding up solid-state battery development. *Nat. Energy* **2023**, *8*, 230–240.

[2] Fan, L. Z.; He, H. C.; Nan, C. W. Tailoring inorganic-polymer composites for the mass production of solid-state batteries. *Nat. Rev. Mater.* **2021**, *6*, 1003–1019.

[3] Wan, J. Y.; Xie, J.; Kong, X.; Liu, Z.; Liu, K.; Shi, F. F.; Pei, A.; Chen, H.; Chen, W.; Chen, J. et al. Ultrathin, flexible, solid polymer composite electrolyte enabled with aligned nanoporous host for lithium batteries. *Nat. Nanotechnol.* **2019**, *14*, 705–711.

[4] Dong, X. R.; Zhang, Y.; You, Z. C.; Chen, Y. M.; Wu, X. W.; Wen, Z. Y. Polyanion-induced single Na-ion polymer electrolytes for ultra-stable sodium metal batteries. *Adv. Funct. Mater.*, in press, DOI: 10.1002/adfm.202405931.

[5] Bao, C. S.; Zheng, C. J.; Zhang, J.; Zhang, Y.; You, Z. C.; Jin, J.; Yuan, H. H.; Wu, M. F.; Wen, Z. Y. A high performance fireproof quasi-solid-state electrolyte enabled by multi-phase synergistic mechanism. *Energy Storage Mater.* **2024**, *68*, 103362.

[6] Han, L. F.; Wang, L.; Chen, Z. H.; Kan, Y. C.; Hu, Y.; Zhang, H.; He, X. M. Incombustible polymer electrolyte boosting safety of solid-state lithium batteries: A review. *Adv. Funct. Mater.* **2023**, *33*, 2300892.

[7] Liu, S. L.; Liu, W. Y.; Ba, D. L.; Zhao, Y. Z.; Ye, Y. H.; Li, Y. Y.; Liu, J. P. Filler-integrated composite polymer electrolyte for solid-state lithium batteries. *Adv. Mater.* **2023**, *35*, 2110423.

[8] Liu, W.; Lee, S. W.; Lin, D. C.; Shi, F. F.; Wang, S.; Sendek, A. D.; Cui, Y. Enhancing ionic conductivity in composite polymer electrolytes with well-aligned ceramic nanowires. *Nat. Energy* **2017**, *2*, 17035.

[9] Li, A. J.; Liao, X. B.; Zhang, H. R.; Shi, L.; Wang, P. Y.; Cheng, Q.; Borovilas, J.; Li, Z. Y.; Huang, W. L.; Fu, Z. X. et al. Nacre-inspired composite electrolytes for load-bearing solid-state lithium-metal batteries. *Adv. Mater.* **2020**, *32*, 1905517.

[10] Wang, W.; Zhou, X. S.; Yu, L.; Liu, L.; Li, X. K.; Zhang, K. W.; Liang, G. M.; Xie, P. T.; Sun, J. K.; Chen, L. et al. Surface sulfidation of NiCo-layered double-hydroxide nanosheets for flexible all-solid-state fiber-shaped asymmetric supercapacitors. *Adv. Compos. Hybrid Mater.* **2023**, *6*, 216.

[11] Yi, P.; Song, Y. Y.; Liu, Z. K.; Xie, P. T.; Liang, G. M.; Liu, R. Z.; Chen, L.; Sun, J. K. Boosting alkaline urea oxidation with a nickel sulfide/cobalt oxide heterojunction catalyst via interface engineering. *Adv. Compos. Hybrid Mater.* **2023**, *6*, 228.

[12] Huo, S. D.; Sheng, L.; Xue, W. D.; Wang, L.; Xu, H.; Zhang, H.; He, X. M. Challenges of polymer electrolyte with wide electrochemical window for high energy solid-state lithium batteries. *InfoMat* **2023**, *5*, e12394.

[13] Liu, X. P.; Xiao, Z.; Peng, H. R.; Jiang, D. T.; Xie, H. G.; Sun, Y. L.; Zhong, S. K.; Qian, Z. F.; Wang, R. H. Rational design of LLZO/polymer solid electrolytes for solid-state batteries. *Chem.—Asian J.* **2022**, *17*, e202200929.

[14] Zhou, D.; Zhang, M. Y.; Sun, F.; Arlt, T.; Frerichs, J. E.; Dong, K.; Wang, J.; Hilger, A.; Wilde, F.; Kolek, M. et al. Performance and behavior of LLZO-based composite polymer electrolyte for lithium metal electrode with high capacity utilization. *Nano Energy* **2020**, *77*, 105196.

[15] Wang, L. C.; Wu, J. X.; Bao, C. S.; You, Z. C.; Lu, Y.; Wen, Z. Y. Interfacial engineering for high-performance garnet-based solid-state lithium batteries. *SusMat* **2024**, *4*, 72–105.

[16] Bao, C. S.; Zheng, C. J.; Wu, M. F.; Zhang, Y.; Jin, J.; Chen, H.; Wen, Z. Y. 12 μm-thick sintered garnet ceramic skeleton enabling high-energy-density solid-state lithium metal batteries. *Adv. Energy Mater.* **2023**, *13*, 2204028.

[17] Sharafi, A.; Kazyak, E.; Davis, A. L.; Yu, S.; Thompson, T.; Siegel,

D. J.; Dasgupta, N. P.; Sakamoto, J. Surface chemistry mechanism of ultra-low interfacial resistance in the solid-state electrolyte $Li_7La_3Zr_2O_{12}$. *Chem. Mater.* **2017**, *29*, 7961–7968.

[18] Huo, H. Y.; Luo, J.; Thangadurai, V.; Guo, X. X.; Nan, C. W.; Sun, X. L. Li_2CO_3: A critical issue for developing solid garnet batteries. *ACS Energy Lett.* **2020**, *5*, 252–262.

[19] Xu, B. Y.; Li, W. L.; Duan, H. N.; Wang, H. J.; Guo, Y. P.; Li, H.; Liu, H. Z. Li_3PO_4-added garnet-type $Li_{6.5}La_3Zr_{1.5}Ta_{0.5}O_{12}$ for Li-dendrite suppression. *J. Power Sources* **2017**, *354*, 68–73.

[20] Kim, Y.; Waluyo, I.; Hunt, A.; Yildiz, B. Avoiding CO_2 improves thermal stability at the interface of $Li_7La_3Zr_2O_{12}$ electrolyte with layered oxide cathodes. *Adv. Energy Mater.* **2022**, *12*, 2102741.

[21] Li, W. W.; Sun, C. Z.; Jin, J.; Li, Y. P.; Chen, C. H.; Wen, Z. Y. Realization of the Li^+ domain diffusion effect via constructing molecular brushes on the LLZTO surface and its application in all-solid-state lithium batteries. *J. Mater. Chem. A* **2019**, *7*, 27304–27312.

[22] Hailu Mengesha, T.; Lemma Beshahwured, S.; Wu, Y. S.; Wu, S. H.; Jose, R.; Yang, C. C. A polydopamine-modified garnet-based polymer-in-ceramic hybrid solid electrolyte membrane for high-safety lithium metal batteries. *Chem. Eng. J.* **2023**, *452*, 139340.

[23] Vema, S.; Sayed, F. N.; Nagendran, S.; Karagoz, B.; Sternemann, C.; Paulus, M.; Held, G.; Grey, C. P. Understanding the surface regeneration and reactivity of garnet solid-state electrolytes. *ACS Energy Lett.* **2023**, *8*, 3476–3484.

[24] Duan, H.; Chen, W. P.; Fan, M.; Wang, W. P.; Yu, L.; Tan, S. J.; Chen, X.; Zhang, Q.; Xin, S.; Wan, L. J. et al. Building an air stable and lithium deposition regulable garnet interface from moderate-temperature conversion chemistry. *Angew. Chem., Int. Ed.* **2020**, *59*, 12069–12075.

[25] Xiong, B. Q.; Nian, Q. S.; Zhao, X.; Chen, Y. W.; Li, Y. C.; Jiang, J. Y.; Jiao, S. H.; Zhan, X. W.; Ren, X. D. Transforming interface chemistry throughout garnet electrolyte for dendrite-free solid-state batteries. *ACS Energy Lett.* **2023**, *8*, 537–544.

[26] Huo, H. Y.; Chen, Y.; Zhao, N.; Lin, X. T.; Luo, J.; Yang, X. F.; Liu, Y. L.; Guo, X. X.; Sun, X. L. *In-situ* formed Li_2CO_3-free garnet/Li interface by rapid acid treatment for dendrite-free solid-state batteries. *Nano Energy* **2019**, *61*, 119–125.

[27] Huo, H. Y.; Li, X. N.; Sun, Y. P.; Lin, X. T.; Doyle-Davis, K.; Liang, J. W.; Gao, X. J.; Li, R. Y.; Huang, H.; Guo, X. X. et al. Li_2CO_3 effects: New insights into polymer/garnet electrolytes for dendrite-free solid lithium batteries. *Nano Energy* **2020**, *73*, 104836.

[28] Li, Y. T.; Xu, B. Y.; Xu, H. H.; Duan, H. N.; Lü, X. J.; Xin, S.; Zhou, W. D.; Xue, L. G.; Fu, G. T.; Manthiram, A. et al. Hybrid polymer/garnet electrolyte with a small interfacial resistance for lithium-ion batteries. *Angew. Chem., Int. Ed.* **2017**, *56*, 753–756.

[29] Dong, S. D.; Zhou, Y.; Hai, C. X.; Zeng, J. B.; Sun, Y. X.; Ma, Y. F.; Shen, Y.; Li, X.; Ren, X. F.; Sun, C. et al. Enhanced cathode performance: Mixed Al_2O_3 and $LiAlO_2$ coating of $Li_{1.2}Ni_{0.13}Co_{0.13}Mn_{0.54}O_2$. *ACS Appl. Mater. Interfaces* **2020**, *12*, 38153–38162.

[30] Negi, R. S.; Yusim, Y.; Pan, R. J.; Ahmed, S.; Volz, K.; Takata, R.; Schmidt, F.; Henss, A.; Elm, M. T. A dry-processed $Al_2O_3/LiAlO_2$ coating for stabilizing the cathode/electrolyte interface in high-Ni NCM-based all-solid-state batteries. *Adv. Mater. Interfaces* **2022**, *9*, 2101428.

[31] Guo, Y. X.; Cheng, J.; Zeng, Z.; Li, Y. Y.; Zhang, H. Q.; Li, D. P.; Ci, L. J. Li_2CO_3: Insights into its blocking effect on Li-ion transfer in garnet composite electrolytes. *ACS Appl. Energy Mater.* **2022**, *5*, 2853–2861.

[32] Wahyudi, W.; Ladelta, V.; Tsetseris, L.; Alsabban, M. M.; Guo, X. R.; Yengel, E.; Faber, H.; Adilbekova, B.; Seitkhan, A.; Emwas, A. H. et al. Lithium-ion desolvation induced by nitrate additives reveals new insights into high performance lithium batteries. *Adv. Funct. Mater.* **2021**, *31*, 2101593.

[33] Paolella, A.; Bertoni, G.; Zhu, W.; Campanella, D.; La Monaca, A.; Girard, G.; Demers, H.; Gheorghe Nita, A. C.; Feng, Z. M.; Vijh, A. et al. Unveiling the cation exchange reaction between the NASICON $Li_{1.5}Al_{0.5}Ge_{1.5}(PO_4)_3$ solid electrolyte and the $pyr_{13}TFSI$ ionic liquid. *J. Am. Chem. Soc.* **2022**, *144*, 3442–3448.

[34] Xiong, S. Z.; Liu, Y. Y.; Jankowski, P.; Liu, Q.; Nitze, F.; Xie, K.; Song, J. X.; Matic, A. Design of a multifunctional interlayer for NASCION-based solid-state Li metal batteries. *Adv. Funct. Mater.* **2020**, *30*, 2001444.

[35] Chae, S.; Williams, L.; Lee, J.; Heron, J. T.; Kioupakis, E. Effects of local compositional and structural disorder on vacancy formation in entropy-stabilized oxides from first-principles. *npj Comput. Mater.* **2022**, *8*, 95.

[36] Yun, H.; Cho, J.; Ryu, S.; Pyo, S.; Kim, H.; Lee, J.; Min, B.; Cho, Y. H.; Seo, H.; Yoo, J. et al. Surface oxygen vacancy inducing Li-ion-conducting percolation network in composite solid electrolytes for all-solid-state lithium-metal batteries. *Small* **2023**, *19*, 2207223.

[37] Song, Y. L.; Yang, L. Y.; Li, J. W.; Zhang, M. Z.; Wang, Y. H.; Li, S. N.; Chen, S. M.; Yang, K.; Xu, K.; Pan, F. Synergistic dissociation-and-trapping effect to promote Li-ion conduction in polymer electrolytes via oxygen vacancies. *Small* **2021**, *17*, 2102039.

[38] Gao, L.; Wu, N.; Deng, N. P.; Li, Z. C.; Li, J. X.; Che, Y.; Cheng, B. W.; Kang, W. M.; Liu, R. P.; Li, Y. T. Optimized CeO_2 nanowires with rich surface oxygen vacancies enable fast Li-ion conduction in composite polymer electrolytes. *Energy Environ. Mater.* **2023**, *6*, e12272.

[39] Ao, X.; Wang, X. T.; Tan, J. W.; Zhang, S. L.; Su, C. L.; Dong, L.; Tang, M. X.; Wang, Z. C.; Tian, B. B.; Wang, H. H. Nanocomposite with fast Li^+ conducting percolation network: Solid polymer electrolyte with Li^+ non-conducting filler. *Nano Energy* **2021**, *79*, 105475.

[40] Kresse, G.; Furthmüller, J. Efficient iterative schemes for *ab initio* total-energy calculations using a plane-wave basis set. *Phys. Rev. B* **1996**, *54*, 11169–11186.

[41] Perdew, J. P.; Burke, K.; Ernzerhof, M. Generalized gradient approximation made simple. *Phys. Rev. Lett.* **1996**, *77*, 3865–3868.

[42] Grimme, S.; Antony, J.; Ehrlich, S.; Krieg, H. A consistent and accurate *ab initio* parametrization of density functional dispersion correction (DFT-D) for the 94 elements H–Pu. *J. Chem. Phys.* **2010**, *132*, 154104.